

## Investigation of polymerization of NVP and drying of PVP in an acoustic levitator using a smart camera for online process measurement

J. Laackmann<sup>1\*</sup>, S. Ahmed<sup>2</sup>, R. Sedelmayer<sup>1</sup>, M. Klaiber<sup>2</sup>, W. Pauer<sup>1</sup>, S. Simon<sup>2</sup>,  
H.-U. Moritz<sup>1</sup>

<sup>1</sup>Institute for Chemical Engineering, University of Hamburg, Germany

<sup>2</sup>Institute of Parallel and Distributed Systems, University of Stuttgart, Germany

julian.laackmann@chemie.uni-hamburg.de and silvia.ahmed@ipvs.uni-stuttgart.de

### Abstract

Spray drying processes combine drying under mild conditions, formation of morphology, and shape forming in one process. These spray drying processes can be supplemented by another unit operation aiming at the production of the dry material, e.g. by polymerization. Since single droplets inside a spray are difficult to study, acoustic levitation is used as a model for spray polymerization. In this study the polymerization of the monomer *N*-vinyl-2-pyrrolidone in levitated droplets was investigated. Competing processes of monomer consumption were observed by imaging and Raman spectroscopy. While the consumption by polymerization could only be monitored using Raman spectroscopy, the evaporation process could be observed by imaging as well as Raman spectroscopy. The results from Raman spectroscopy in conjunction with principal components analysis were backed up by image analysis. Because of bandwidth and memory limitations the image analysis was done offline. In order to reduce bandwidth and memory usage, an algorithm was developed that enables droplet features like surface area and volume to be measured online in a single pass. For this algorithm, a suited architecture was derived and implemented on the FPGA of a smart camera. The general feasibility of employing such a smart camera is demonstrated on images obtained by shadowgraphy during acoustic levitation.

---

### Introduction

Spray processes are known since the 19th century [1] and are nowadays widely used in the pharmaceutical and chemical industries to remove solvents from thermolabile compounds. By generating droplets from solutions, dispersions or emulsions, an enlargement of the surface is achieved. For instance 1 m<sup>3</sup> of substance, sprayed into droplets with a diameter of 100 μm, results in a total surface of 6 · 10<sup>4</sup> m<sup>2</sup>, which leads to high mass and heat transfer rates. When the spray moves through the heated drying gas the droplets do not reach temperatures higher than the wet-bulb temperature of the solvent (as long as there is solvent left) because of the enthalpy of vaporization. This leads to mild drying conditions even if the temperature is higher than the decomposition temperature of the compound. In most of the dryers the gas flow and the spray move in the same direction [2]. In this cocurrent design the spray sees the highest temperature at the top of the tower, where it is still wetted, and lower temperatures at the bottom of the tower, where a heat exchange with the environment has taken place and the compound is dried. In general spray processes operate under mild drying conditions and combine several unit operations like removal of solvent, formation of morphology and shape forming in one process. The spray drying process can be supplemented by another unit operation aiming at the preparation of the dry material before the drying process. This unit operation may consist of a polymerization reaction that occurs mainly in the first part of the spray tower and produces the wet product that is subsequently dried, e.g. [3].

Most of these unit operations depend strongly on the conditions inside the spray tower, i.e. temperature and relative humidity of the drying gas. In contrast to the analytics of the starting materials and the obtained particles, analyzing the processes inside the spray tower is challenging. Investigations of spray properties are usually limited to statistical considerations since the positions of the instruments are fixed and the spray can only be described as a basic population, e.g. [4]. Acoustic levitation is used to investigate single droplets during the drying process. By generating a standing acoustic wave the gravitational force is compensated and droplets or particles can be positioned containerlessly. The principle of acoustic levitation is known and well described in literature since 1934, e.g. [5, 6, 7].

Observing the conversion of monomer during the polymerization reaction, e.g. by Raman spectroscopy, generates a large amount of information since every spectrum contains *k* values displaying the intensities of the Raman shifts. In order to reduce the information of *n* spectra with *k* values each principal component analysis (PCA) can

---

\*Corresponding author: julian.laackmann@chemie.uni-hamburg.de

be applied. This method was first published in 1901 by PEARSON [8] and rediscovered over the years in different sciences [9]. To reduce the information of the  $(n \times k)$ -matrix linear combinations of the variables, called principal components, are used which represent the effects of the measurement.

In order to monitor the evaporation of levitated droplets shadowgraphy is usually employed. A camera records the shadow of the droplet in front of an illuminated background and allows deriving the geometry of the droplet from the images. These measurements are done online to avoid generating too much overhead and saving bandwidth as well as memory. The basic principle for obtaining the required data to calculate the geometry of the droplets on the first pass has been mentioned in [10]. To do so, the various moment invariants need to be calculated from the image. The use of image moment invariants for pattern recognition was first introduced by HU in 1962 [11]. Since then, numerous works like [12], [13], and [14] have been devoted to various improvements and generalizations of HU's invariants and to its use in different application areas. In this paper, the various moment invariants of the images were utilized to fit the ellipsoid, considering that the droplet shadow is more likely to be similar to ellipses than to circles. From raw pixel data acquisition to the final calculation of the droplet characteristics, all necessary steps are done in single pass without the need of actually storing the image. Thus the resulting hardware architecture ensures high performance with minimum memory requirement which is able to acquire the droplet features in single pass.

In this context a smart camera system with integrated processing capabilities is introduced to compute droplet characteristics from the images online. The required algorithm was implemented in parallel on the field-programmable gate array (FPGA) which is connected to the image sensor of the camera. Therefore the name 'smart camera' is used. Since the pixel stream is processed inside the camera and only relevant information is passed on, real-time measurements with high frame rates are feasible.

## Experimental and Numerical Methods

### *Materials and Experimental Setup*

All substances were used as received. *N*-vinyl-2-pyrrolidone (NVP) was purchased from Acros Organics and 2,2'-azobis[2-(2-imidazolin-2-yl)propane]dihydrochloride (VA-044) was donated by BASF.

Polymerizations were performed using 20 %wt of NVP and 0.25 %mol of VA-044 related to NVP in water. The solution was rendered inert by purging with gaseous nitrogen. The droplet was inserted into the acoustic field, which was established under inert conditions at an ambient temperature of 70 °C. Afterwards imaging and Raman spectroscopy were started. The evaporation of the solvent and the monomer were observed by the camera, the consumption of monomer by Raman spectroscopy.

The droplet levitation experiments were carried out using a custom built acoustic levitator working at a frequency of 40 kHz. The transducer and reflector were surrounded by a process chamber to guarantee defined conditions around the levitated droplet. The desired temperature was achieved by a heating band on the outside of the process chamber as well as applying a heated gas flow (approx. 0.02 m/s). Temperature and relative humidity were measured inside the process chamber with a Pt100 and a HMT337 humidity probe (VAISALA) respectively.

Images of the levitated droplet were taken with a PL-A741 CMOS camera (PixeLINK). In order to enable simultaneous imaging and Raman spectroscopy a pulsed LED light source was used. The light source Tiny'z (Laser2000) contained twelve high power LEDs which were positioned in a circle around the objective lens. Camera and light source were triggered with a frequency of 1 Hz during the experiments.

Raman spectra were obtained with a Raman spectroscope RA100 (Renishaw) employing a diode laser with a wavelength of 785 nm and a Raman probe (InPhotonics Inc.) with a focal length of 1 cm. In order to avoid burning of the sample, the power of the laser was limited to 50 mW. The Raman probe was positioned opposite of the camera with the levitated droplet in between. Spectra with an integration time of 2 s were recorded every 3 s.

### *Data Processing*

The Raman spectra were preprocessed by adding ten consecutive spectra each to reduce the noise. Similar to the smoothing algorithm proposed by SAVITZKY and GOLAY [15] the next set of ten spectra is shifted by one spectrum on the time scale. This moving sum algorithm leads to an improved temporal resolution compared to regarding the sum of ten spectra and then move on to the next ten spectra as it is often done in literature. For the case of one spectrum every 3 s and an accumulation of ten spectra this results in a temporal resolution of one spectrum every 3 s instead of one spectrum every 30 s. The accumulated spectra were baseline corrected by subtracting a fitted function and then normalized by standard normal variate (SNV) in order to neglect the decrease

in intensity (Equation (1)).

$$\hat{x} = \frac{x_k - \bar{x}}{\sigma(x)} \quad (1)$$

The SNV corrected spectrum  $\hat{x}$  in Equation (1) is calculated from the mean  $\bar{x}$  of the original spectrum  $x_k$  and the standard deviation  $\sigma(x)$ .

The PCA was performed on the SNV and baseline corrected data using The Unscrambler X (Camo).

The image analysis of the polymerization experiment was done manually by fitting an ellipse over the droplet image in ImageJ and computing the surface  $A$  of an ellipsoid with the major axis  $r_{maj}$  and the minor axis  $r_{min}$  (Equation (2)). In order to facilitate the image analysis the contrast of the obtained images was enhanced with Matlab.

$$A = 2\pi r_{maj}^2 \left( 1 + \left( \frac{r_{min}}{r_{maj}} \right)^2 \frac{\operatorname{arctanh} \epsilon}{\epsilon} \right), \quad \text{with} \quad \epsilon = \sqrt{1 - \left( \frac{r_{min}}{r_{maj}} \right)^2} \quad (2)$$

The evaporation coefficient  $\beta$ , proposed in [16], was modified to account for the ellipsoidal geometry of the droplet.

$$\beta = \frac{dA}{dt} \quad (3)$$

### **Elliptical Feature Extraction**

As mentioned above, the shape of the droplets can be described best as being elliptical. The elliptical feature extraction is a well-known method for pattern-recognition and has been described in [12], [17], and [18]. The  $(p+q)$ th order two-dimensional geometric moments of an image intensity function  $f(x, y)$  which is defined on the region  $D$  can be expressed as [19]:

$$m_{pq} = \iint_D f(x, y) x^p y^q dx dy \quad (4)$$

where  $x$  is the column value and  $y$  is the row value of the corresponding pixel.

The gray-level images are thresholded and binary images are obtained, i.e.  $f(x, y)$  has the value of '1' on the object region  $D$ . Since  $f(x, y)$  is a digital image, the double integral in Equation (4) equals the sum of the column and row values to the  $p$ th and  $q$ th power respectively [17]. For the binary images, Equation (4) becomes:

$$m_{pq} = \sum_D x^p y^q \quad (5)$$

Translation of the image by vector  $(-x_t, -y_t)$  creates a centered image where  $x_t = \frac{m_{10}}{m_{00}}$  and  $y_t = \frac{m_{01}}{m_{00}}$  are centroid coordinates. The moments computed with respect to these object centroids are called central moments and are defined as:

$$\mu_{pq} = \sum_D (x - x_t)^p (y - y_t)^q \quad (6)$$

A convenient representation of the droplet shadow can be provided by an ellipse that is centered at the centroid coordinates of the droplet. The second-order central moments commonly known as the covariances build a covariance matrix  $\begin{bmatrix} \mu_{20} & \mu_{11} \\ \mu_{11} & \mu_{02} \end{bmatrix}$ . The eigenvectors of this covariance matrix can be found either by diagonalizing this matrix by principal component analysis or by applying Equation (7) directly:

$$\lambda_{l,s} = \frac{\mu_{20} + \mu_{02} \pm \sqrt{(\mu_{20} + \mu_{02})^2 + 4\mu_{11}^2}}{2} \quad (7)$$

The droplet shadow is approximated in the coordinate system of the normalized position of the region by an ellipse with the semi-axes  $r_{maj}$  and  $r_{min}$ .

$$\frac{x^2}{r_{maj}^2} + \frac{y^2}{r_{min}^2} = 1, \quad \text{with } r_{maj} = 2\sqrt{\lambda_l}, \quad r_{min} = 2\sqrt{\lambda_s} \quad \text{and } r_{maj} \geq r_{min} > 0, \quad (8)$$

The surface of the droplet is obtained by applying Equation (2).

### Single Pass Mechanism

From Equation (6), all three second-order moments can be extracted with the number of pixels  $N$  that has the value of '1' in the droplet region of the image:

$$\begin{aligned} \mu_{20} &= \frac{1}{N} \sum_{i=1}^N (x_i - x_t)^2 = \frac{1}{N} \left[ \sum_{i=1}^N x_i^2 - \frac{1}{N} \left( \sum_{i=1}^N x_i \right)^2 \right] \\ \mu_{02} &= \frac{1}{N} \sum_{i=1}^N (y_i - y_t)^2 = \frac{1}{N} \left[ \sum_{i=1}^N y_i^2 - \frac{1}{N} \left( \sum_{i=1}^N y_i \right)^2 \right] \\ \mu_{11} &= \frac{1}{N} \sum_{i=1}^N (x_i - x_t)(y_i - y_t) = \frac{1}{N} \left[ \sum_{i=1}^N x_i y_i - \frac{1}{N} \left( \sum_{i=1}^N x_i \right) \left( \sum_{i=1}^N y_i \right) \right] \end{aligned} \quad (9)$$

Each of these expressions requires multiplication(s) and then addition and subtraction whenever the pixel value is '1' in  $D$ . In terms of hardware, this makes the architecture fairly expensive both in terms of resources and speed. The summations of multiplication (e.g.  $\sum x^2$ ) contained in these equations can be accumulated also by using incremental calculations without implementing any multiplier. The sum of the squares of the first  $n$  natural numbers can be expressed as:

$$\sum_{k=1}^n x_k^2 = x_1^2 + x_2^2 + \dots + x_n^2 = \sum_{k=1}^{n-1} x_k^2 + x_n^2 \quad (10)$$

Equation (10) can be applied for one row of an image where  $n$  is the number of columns. The first squared value in the first column is '1' ( $x_1^2 = 1^2 = 1$ ). The consecutive squared terms can be obtained from Equation (11), where it is enough to store the square of the current column value of the corresponding pixel and then perform some additions and bit-shift to get the next squared term. The squared term attained in this way is added to the summation only if the corresponding pixel value is '1'.

$$x_n^2 = (x_{n-1} + 1)^2 = x_{n-1}^2 + 2x_{n-1} + 1 \quad (11)$$

After finishing calculation of a row, the result can be accumulated into the temporary sum, the initial squared result (i.e.  $x_1^2$ ) can be reset to '1' and the same procedure from Equation (10) and (11) may follow for the next row. This minimizes the requirement of hardware resources, making the entire architecture less hardware expensive while maintaining the high performance of the system.

After the covariance matrix is formed for one ellipsoidal droplet, a dedicated architecture can then be used to perform the necessary calculation of Equations (7) and (8). At the same time, the incremental calculation is continued in parallel for the next droplet with the summation parameters ( $\sum 1, \sum x, \sum y, \sum x^2, \sum y^2$  and  $\sum xy$ ) reset to zeros. Thus, this system is able to extract the droplet features as soon as the pixels of one droplet are obtained from the image sensor and passed on as the output instead of the entire image. This minimizes the memory requirement and the transmission bandwidth to a great extent.

### Results and Discussion

The images in Figure 1 display the levitated droplet in front of the Raman probe. Because of the magnification of the objective lens only a part of the laser/detector window of the Raman probe was visible. The ring light was

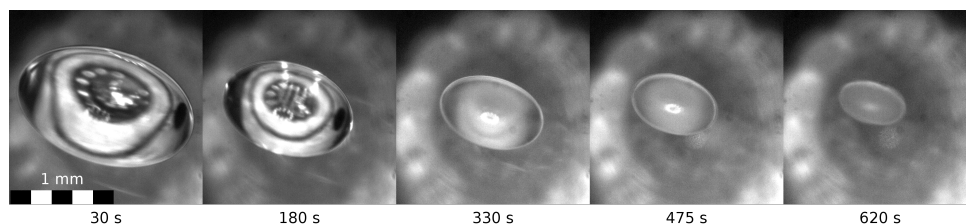


**Figure 1.** Contrast adjusted images of the levitated droplet at different times. On the droplet and in the background the LED ring light is reflected.

reflected on the droplet as well as on the Raman probe, where it was blurred since the Raman probe was not in the focal plane. The increase in brightness of the image at 180 s compared to the one at 330 s resulted from the contrast adjusting algorithm which remaps the intensity values of the pixels in such a manner, that 1 % of the pixels are saturated at low and high intensities. Since there were less dark pixels in the latter images remapping led to brighter images. The deformation of the droplet arose from the acoustic forces which are three to six times larger in the radial than in the axial direction [6]. After approximately 230 s (images not shown) the droplet became opaque and kept its appearance until the end of the experiment. The opacity evolved at the same time the evaporation of the water was nearly completed and only 25 %vol of the applied droplet were left.

With the help of the images the surface was computed offline and plotted versus time (Figure 2, squares). The decrease of the surface, which is correlated with the droplet size, proceeded in two phases with different evaporation coefficients. During the first 249 s the evaporation coefficient  $\beta$  amounted to  $19 \cdot 10^3 \mu\text{m}^2/\text{s}$  and diminished then to  $5.0 \cdot 10^3 \mu\text{m}^2/\text{s}$ . The transition from the first phase to the second was well defined and lasted less than one minute. Both phases were described by linear functions over time as expected from the  $d^2$ -law [20]. The experimental data were fitted with two linear functions, one for each evaporation phase (Figure 2, solid lines).

In order to detect mixed evaporation coefficients, droplets of pure solvent and pure monomer were evaporated. The conditions of these experiments were similar to those of the polymerization experiments. For water, five experiments were averaged and for NVP eight. Plotting the surface versus time showed a considerably higher evaporation coefficient for water (Figure 2, dashed line,  $20 \cdot 10^3 \mu\text{m}^2/\text{s}$ ) than for NVP (dot-dashed line,  $5.2 \cdot 10^3 \mu\text{m}^2/\text{s}$ ). Comparing the fitted data of the polymerization experiments to the evaporation coefficients of the pure solvent and monomer the first phase was assigned to the evaporation of water and the second to the evaporation of NVP with a deviation of only 5 % and 4 % respectively.

Raman spectra of the levitated droplet obtained at 12, 249 and 468 s are shown in Figure 3. After 12 s the spectrum of the levitated droplet differed significantly from the spectrum of pure NVP. The sharp double peak at  $1615$  and  $1679 \text{ cm}^{-1}$  originating from the C=C stretching vibration of the vinyl group of NVP was shifted (Figure 3a). In addition, several peaks at lower Raman shifts were shifted and exhibited different intensities.

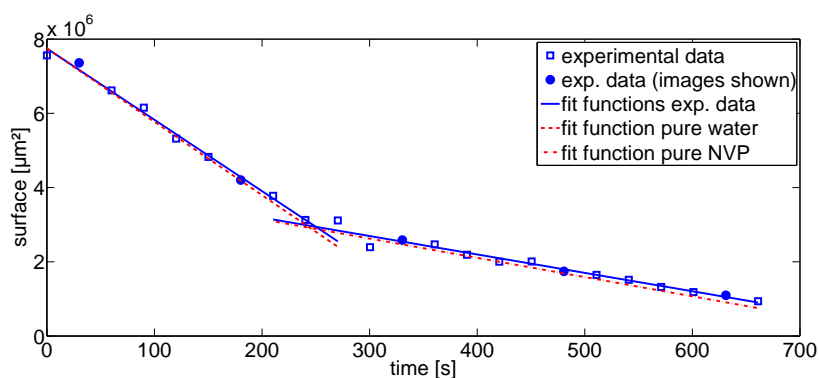


**Figure 2.** Surface of the levitated droplet and the fitted functions for the first and second evaporation phases of the levitated droplet (solid lines) as well as pure water (dashed line) and NVP (dash-dotted lines). Points describing the images in Figure 1 are represented by filled circles (●).

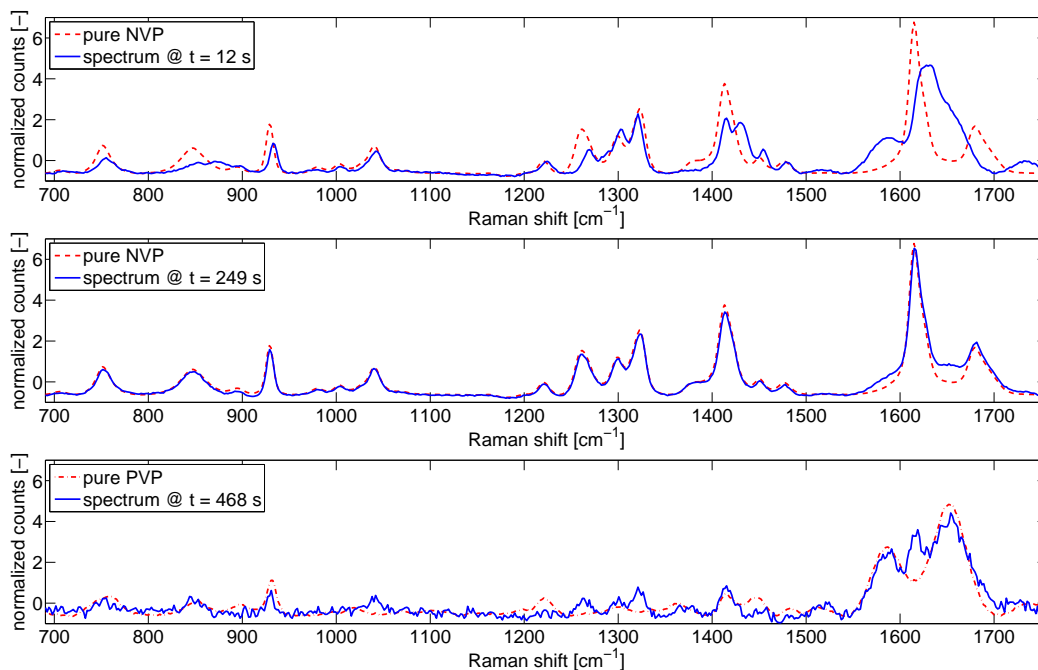


**Figure 3.** Raman spectra of the polymerization (solid lines) after a) 12 s, b) 249 s and c) 468 s as well as pure spectra (dashed lines) of a,b) NVP and c) PVP.

After 249 s, when the evaporation of water was almost completed as derived from the droplet size (Figure 2), the spectrum was nearly identical to the spectrum of pure NVP (Figure 3b). Only the small shoulders of the peak at 1615 cm<sup>-1</sup> indicated the conversion of NVP to PVP. After 468 s the polymerization of NVP had obviously progressed. Despite the remaining peak at 1615 cm<sup>-1</sup> the spectrum resembled that of pure PVP (Figure 3c).

The results gained from Raman spectroscopy were analyzed by PCA. The first principal component (PC1) accounted for 53 % of the variance within the Raman spectra and described mainly the formation of the NVP spectrum. The second principal component (PC2) accounted for 42 % of the variance and explained primarily the formation of the PVP spectrum. In Figure 4 the scores and loadings of PC1 and PC2 are shown. Starting below average on PC1 the spectra evolved in the direction of the pure NVP spectrum. In the first 60 s the spectra evolved additionally on PC2 since the spectra of aqueous NVP were slightly similar to the spectrum of pure PVP. Spectra taken near the end of the water evaporation (249 s) accumulated in a cluster that was above average on PC1 and average on PC2. From this point on the spectra developed on a straight line which connected the pure spectra of NVP and PVP describing the polymerization process.

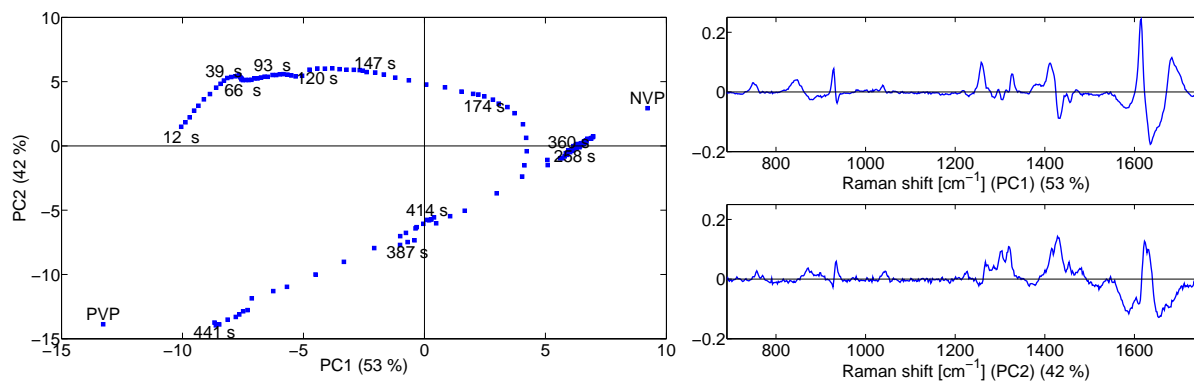


**Figure 4.** Scores (left) and loadings (right) of PC1 and PC2.

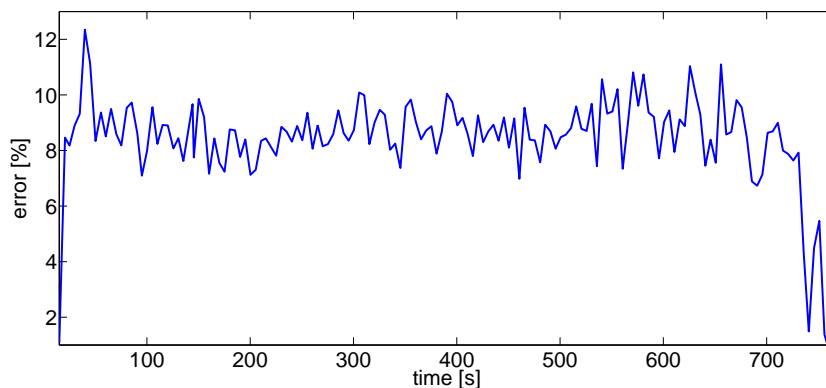


**Figure 5.** Error in the computation of the droplet surface between the offline analysis using the LabVIEW image processing library and the online processing based on a simplified binarization with the proposed algorithm implemented on the smart camera.

In order to prove the feasibility of real-time image analysis by an algorithm implemented on a smart camera, images obtained by shadowgraphy were analyzed. After the levitation started, images were taken every 5 seconds for 750 seconds. The geometry of the droplet was deduced from the image of the droplet shadow and the surface was calculated using Equation (2). The average error in the computation of the surface by this architecture amounted to 8.3 % (Figure 5). The uniformity of the variance indicates a bias that resulted from image binarization. The performance of this design can be further enhanced to process 100 Mega-Pixels per second or more with the current architecture by pipelining as the proposed algorithm contains no feedback loops.

### Summary and Conclusions

The investigation of the polymerization of NVP inside levitated droplets showed the competition between monomer and solvent evaporation and the polymerization of monomer. While the consumption of monomer by polymerization is desirable to yield the polymer which is subsequently dried, the evaporation of the monomer is highly undesirable. Not only is the overall conversion reduced, but the transfer rate of the monomer into the gaseous phase inside the spray tower is unnecessarily increased. From a safety point of view, enrichment of monomer above the explosion limit is in general highly dangerous, especially inside a heated spray tower. Since the risk of explosion of the used monomer NVP is very low this issue was of no concern in the recent study.

Analyzing the droplet surface during the experiment revealed that the evaporation of the solvent preceded the evaporation of the monomer. Since the evaporation of the solvent was four times faster than the evaporation of the monomer, removing the solvent was completed before the polymerization was finished. The images taken during the experiments displayed opacity of the initially translucent droplet which evolved at the same time the water evaporation was nearly completed. Raman spectroscopy in conjunction with PCA was used to distinguish between evaporation and polymerization inside the levitated droplet and the results were backed up image analysis. Prediction of the conversion with the help of Raman spectra was not possible, but providing a proper PLS model can solve this problem in the future. Especially tracing the evaporation process in Raman spectroscopy is noteworthy since this enables the observation of both competing processes with only one analytical method.

Instead of obtaining the image of the droplet and analyzing its geometry offline, a hardware architecture and suited algorithm was proposed and implemented on an FPGA inside a camera for online analysis. The usage of such a smart camera was successfully exploited in the evaporation process. The entire algorithm was developed in such a way that the analysis was done in a single pass that in turn minimized the bandwidth and memory requirement of the resulting system. The architecture and algorithm of this camera will be extended in the future to observe the formation of the morphology and shape of the particles.

### Acknowledgements

The authors would like to thank the German Research Foundation (DFG) for funding this research in the scope of SPP 1423 Prozess-Spray and JL would like to thank BASF for donating VA-044.

## References

- [1] S. R. Percy, "Improvement in drying and concentrating liquid substances by atomizing," Patent US 125 406, 1872.
- [2] L. Huang, K. Kumar, and A. S. Mujumdar, "A parametric study of the gas flow patterns and drying performance of co-current spray dryer results of a computational fluid dynamics study," *Drying Technol.*, vol. 21, pp. 957–978, 2003.
- [3] M. Schmid, V. Seidl, D. Distler, H.-J. Hähnle, D. Lösch, H.-U. Moritz, and M. Krüger, "Spray polymerisation of radically-polymerisable monomer solution for production of absorbent polymer for use in hygiene articles, involves using monomer solution with a water content of at least 55 wt. percent," Patent DE 10 340 253 A1, 2005.
- [4] F. Dannigkeit, L. Steinke, and S. Ripperger, "Inline-measurement of mean droplet diameter and droplet concentration of process sprays," *Chem. Ing. Tech.*, vol. 84, pp. 357–364, 2012.
- [5] L. V. King, "On the acoustic radiation pressure on spheres," *P. Roy. Soc. Lond. A Mat.*, vol. 147, pp. 212–240, 1934.
- [6] E. G. Lierke, "Acoustic levitation – a comprehensive survey of principles and applications," *Acta Acust.*, vol. 82, pp. 220–237, 1996.
- [7] A. L. Yarin, M. Pfaffenlehner, and C. Tropea, "On the acoustic levitation of droplets," *J. Fluid Mech.*, vol. 356, pp. 65–91, 1998.
- [8] K. Pearson, "On lines and planes of closest fit to systems of points in space," *Philos. Mag.*, vol. 2, pp. 559–572, 1901.
- [9] S. Wold, K. Esbensen, and P. Geladi, "Principal component analysis," *Chemometr. Intell. Lab.*, vol. 2, pp. 37–52, 1987.
- [10] D. G. Bailey, *Design for Embedded Image Processing on FPGAs*. John Wiley & Sons (Asia) Pte Ltd, 2011.
- [11] M.-K. Hu, "Visual pattern recognition by moment invariants," *Information Theory, IRE Transactions on*, vol. 8, pp. 179–187, 1962.
- [12] M. R. Teague, "Image analysis via the general theory of moments\*," *J. Opt. Soc. Am.*, vol. 70, pp. 920–930, 1980.
- [13] F. Chaumette, "Image moments: a general and useful set of features for visual servoing," *Robotics, IEEE Transactions on*, vol. 20, pp. 713–723, 2004.
- [14] K. Mulchrone, "Fitting an ellipse to an arbitrary shape: implications for strain analysis," *Journal of Structural Geology*, vol. 26, pp. 143–153, 2004.
- [15] A. Savitzky and M. J. E. Golay, "Smoothing and differentiation of data by simplified least squares procedures," *Anal. Chem.*, vol. 36, pp. 1627–1639, 1964.
- [16] A. Brask, T. Ullum, P. Thybo, and M. Wahlberg, "High-temperature ultrasonic levitator for investigating drying kinetics of single droplets," Niro A\ S, Tech. Rep., 2007.
- [17] L. Rocha, L. Velho, and P. Carvalho, "Motion reconstruction using moments analysis," in *Computer Graphics and Image Processing, 2004. Proceedings. 17th Brazilian Symposium on*, 2004, pp. 354–361.
- [18] J. Sedlar, B. Zitova, J. Kopecek, T. Todorciuc, and I. Kratochvilova, "Detection of elliptical particles in atomic force microscopy images," in *Acoustics, Speech and Signal Processing (ICASSP), 2011 IEEE International Conference on*, 2011, pp. 1233–1236.
- [19] J. Flusser, B. Zitova, and T. Suk, *Moments and Moment Invariants in Pattern Recognition*. Wiley Publishing, 2009.
- [20] R. Vehring, "Pharmaceutical particle engineering via spray drying," *Pharm. Res.*, vol. 25, pp. 999–1022, 2007.